PERGAMON

Acta mater. Vol. 47, No. 13, pp. 3579–3588, 1999
© 1999 Acta Metallurgica Inc.
Published by Elsevier Science Ltd. All rights reserved.
Printed in Great Britain
1359-6454/99 $20.00 + 0.00

PII: S1359-6454(99)00221-9

DISLOCATION STABILITY AND DEFORMATION MECHANISMS OF IRON ALUMINIDES AND SILICIDE

M. H. YOO[1]†, K. YOSHIMI[1] and S. HANADA[2]

[1]Metals and Ceramics Division, Oak Ridge National Laboratory, Oak Ridge, TN 37831-6115, U.S.A. and [2]Institute for Materials Research, Tohoku University, Sendai 980-77, Japan

(Received 25 June 1999; accepted 16 July 1999)

Abstract—Elastic stability of dislocations in FeAl alloys and Fe_3Si was examined with respect to the formation of jog pair(s) on a straight dislocation as well as the kink-pair formation. Dislocation configurations from annealed and deformed microstructures available in the literature are consistent with the predictions based on elastic instability. The difference in the formation enthalpy between a jog pair and a kink pair was obtained, and the activation enthalpy of a jog-pair pinning mechanism for edge dislocations was prescribed. Discussion is given on the driving forces for the pinning mechanisms, including the role of inhomogeneous internal stress in FeAl single crystals. *© 1999 Acta Metallurgica Inc. Published by Elsevier Science Ltd. All rights reserved.*

Keywords: Iron; Theory; Elastic; Thermally activated processes; Line tension

1. INTRODUCTION

Iron-rich iron aluminides have been investigated extensively in the present decade as one of the candidates for high-temperature structural applications because of their excellent oxidation and corrosion resistance, relatively good high-temperature strength, low mass density, and low cost [1, 2]. As alloy design and development activities have intensified, our effort to understand dislocation mechanisms responsible for the deformation behavior of iron aluminides, such as the vacancy hardening and the yield stress anomaly, has also increased. The excess vacancy hardening was recognized in the 1960s [3], but since the recent work on the composition and cooling rate dependence of hardness of B2 FeAl [4], special attention has been given to iron aluminides recently. It is now well established that a positive temperature dependence of yield stress appears unambiguously after eliminating the effect of excess vacancy strengthening [5, 6]. A number of mechanisms for yield strength anomaly have been proposed based on experimental findings [7–12], but a dislocation mechanism that can account for both yield stress anomaly and excess vacancy hardening in FeAl alloys has not been fully developed.

Stability of dislocations in FeAl alloys plays an important role in deformation mechanisms for yielding and work hardening. From their weak-beam transmission electron microscopy (TEM) investigation, Crawford *et al.* [13] reported that a [111] dislocation in Fe–36 at.% Al (hereafter, Fe–36Al) is dissociated into two superpartials, [111]/2, on the $(1\bar{1}0)$ slip plane, the antiphase boundary (APB) energy is $\Gamma_{110} = 110\ \mathrm{mJ/m^2}$, and the superpartials are unstable over a certain angular range of the dislocation line orientation due to the elastic anisotropy. The elastic constants of Fe–(4–40)Al alloys at low temperatures [14] and Fe–30Al at elevated temperatures [15] indicate that the negative line tension occurs in the $(1\bar{1}0)[111]$ slip system over wide ranges of composition and temperature. The spacing between superpartials in B2 and $D0_3$ alloys determined by TEM analyses [13, 16, 17] is much larger (>5 and >3 nm, respectively, at the edge and screw orientations) than that corresponding to the theoretical value of $\Gamma_{110} = 300\ \mathrm{mJ/m^2}$ for stoichiometric FeAl at 0 K [18]. This indicates that both the elastic constants and APB energies depend sensitively on the alloy composition and temperature.

Glide decomposition of $[111] \rightarrow [001] + [110]$ is predicted to occur along the near-edge orientations ($54.7^\circ < \theta < 144.7^\circ$ between the [001] and [110] directions) in the $(1\bar{1}0)$ plane of B2 alloys with a high APB energy such as NiAl [19]. The repulsive interaction between the two resultants over the angular range is due entirely to the mutually perpendicular Burgers vectors, not due to the elastic anisotropy. In spite of the relatively low APB energies, glide decomposition of [111] is possible in Fe–39Al deformed at 823 K which is just below the peak temperature of the yield stress anomaly [20]. The slip vector transition form $\langle 111 \rangle$ to $\langle 100 \rangle$ near the peak temperature depends also on the alloy composition [21, 22]. Based on their TEM analysis

†To whom all correspondence should be addressed.

of the 'quenched-in' dislocation substructure in Fe–28Al–2Cr–0.5Zr and Fe–37Al–0.2Mo alloys, Kad and Horton [23] concluded that ⟨111⟩ dislocations are the dominant slip vectors at elevated temperatures (925–1325 K), not ⟨100⟩ dislocations.

Since dislocations are sources and sinks for thermal vacancies, the immobilization of a glide dislocation resulting from point defect–dislocation interactions is important for deformation behavior of FeAl alloys. The purpose of this paper is to analyze the stability of dislocations in FeAl alloys and Fe_3Si, not only with respect to kink pairs on glide dislocations but also to jog pairs on them, and to develop dislocation mechanisms for the formation of pinning points on glide dislocations in order to explain the reported deformation behavior.

2. DISLOCATION LINE INSTABILITY

An overview on the influence of elastic anisotropy on dislocation instability was given recently by Wang and Lothe [24]. The numerical method used for calculating the energy factors (K) of straight dislocations and the line tension (T_L) of planar curved dislocations is described in the Appendix, and the calculated results are given below. The calculations were made using the measured elastic constants of iron aluminides [14, 15], and of α-Fe [25] and Fe_3Si [26] for comparison purposes. Table 1 lists the elastic constants and the two anisotropy factors, $A = 2C_{44}/(C_{11} - C_{12})$ and $H = 2C_{44} - C_{11} + C_{12}$, for α-Fe, Fe_3Si, and five FeAl alloys at room temperature and also for α-Fe and Fe–30Al at 773 K.

2.1. Glide dislocation—shear loop

A rotation of the Cartesian coordinate system for a straight dislocation is described in Fig. 1, where the angle θ is measured from the Burgers vector to the dislocation line direction. The inverse energy factor plots ($1/K$ vs θ) for $(1\bar{1}0)[111]$ slip in Fe–40Al, Fe–34Al, and Fe–25Al at room temperature are shown in Fig. 2. If the logarithmic term in the expression for dislocation line energy [equation (A1) in the Appendix] is assumed to be a constant for all dislocation orientations, then the $1/K$ plots

Table 1. Elastic stiffness constants and anisotropy factors of iron aluminides and silicide at room temperature

Alloys	C_{11}	(10^2 GPa) C_{12}	C_{44}	(10^2 GPa) A	H
α-Fe	2.26	1.40	1.16	2.70	1.46
α-Fe[a]	2.00	1.22	1.05	2.69	1.32
25Si	2.32	1.56	1.35	3.55	1.94
40Al	1.81	1.14	1.27	3.77	1.87
34Al	1.72	1.14	1.30	4.46	2.01
30Al	1.47	0.96	1.16	4.59	1.82
30Al[a]	1.18	0.84	0.95	5.58	1.56
28Al	1.66	1.23	1.31	5.98	2.18
25Al	1.71	1.31	1.32	6.52	2.23

[a] At 773 K.

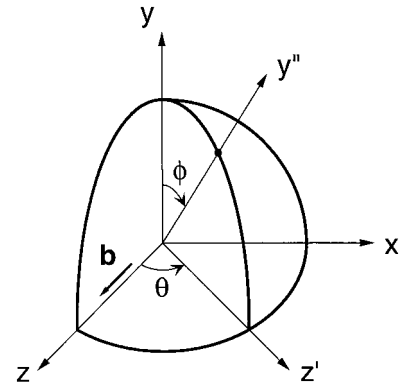

Fig. 1. Right-handed Cartesian coordinate system for a straight dislocation. Burgers vector, **b**, is parallel to the z-axis. The dislocation line vector, **t**, is parallel to the z'-axis after a rotation of the coordinate system by θ about the y-axis and then to the z''-axis after a rotation by ϕ about the x'-axis.

are equivalent to the inverse Wulff ($1/E$) plots of the corresponding line energies [27]. There are two criteria for dislocation line instability [28], (a) the concavity of an inverse Wulff plot, and (b) the negative line tension ($T_L < 0$ of equation (A7) in the Appendix). According to the former, dislocations in Fe_3Al lying within the angular range of $25° < \theta < 75°$, which is defined by the two common tangent points (A and B) made by a straight line shown in Fig. 2, are unstable. The second criterion applied to Fe_3Al gives the angular range of $37° < \theta < 60°$ which is defined by the two inflection points (P and Q) shown in Fig. 2. Table 2 lists these two angular ranges for the nine different cases. Negative line tension, $K(\theta) + K''(\theta) < 0$, is a sufficient but not necessary condition for instability [24, 27]. For instance, dislocations with orientations in the range AP or QB are unstable although the line tension is positive. Consequently, all straight dislocations within the larger interval θ_A–θ_B will relax their energy by transforming into a V-shaped bend or zigzag (Z-shaped) bends [24, 27].

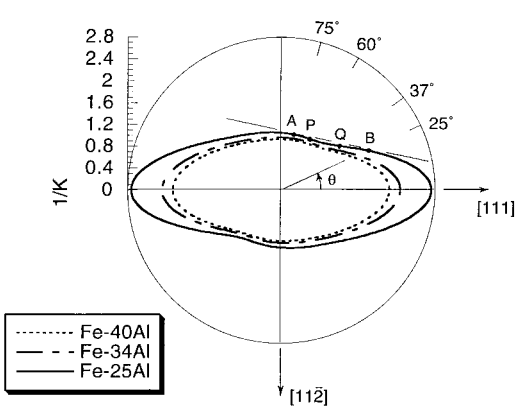

Fig. 2. Inverse energy factor plot for a $(1\bar{1}0)[111]$ glide loop in three FeAl alloys at room temperature, where θ is the angle between the Burgers vector and the dislocation line direction and K is the dislocation energy factor.

Table 2. Angular ranges of elastic instability of glide dislocations on the (110) slip plane at room temperature. The angle θ is in deg measured counterclockwise from the slip vector

Alloys	[111]		[001]			
			$\theta = 0°$		$\theta = 90°$	
	θ_A–θ_B	θ_P–θ_Q	A–B	P–Q	A–B	P–Q
α-Fe	–	–	±25	±10	–	–
α-Fe[a]	–	–	±18	±10	–	–
25Si	25–59	39–54	±18	±13	–	–
40Al	25–61	38–55	±29	±14	–	–
34Al	25–68	37–57	±32	±15	–	–
30Al	25–72	37–58	±32	±15	±11	±1
30Al[a]	25–72	37–59	±35	±15	±18	±10
28Al	25–66	37–60	±35	±15	±21	±12
25Al	25–75	37–60	±36	±15	±24	±13

[a] At 773 K.

Figure 3 shows the $1/K$ plots for $(1\bar{1}0)[001]$ slip in the three representative alloys. In this case, there are two different ranges of instability, one centered on $\theta = 0°$ (screw) and the other on $\theta = 90°$ (edge). The angular ranges for elastic instability in all nine cases are listed in Table 2. The $1/K$ plots for $(1\bar{1}0)[110]$ slip shown in Fig. 4 are convex everywhere, so glide dislocations of this slip system are stable in all orientations. Figure 5 gives the $1/K$ plots for (001)[010] slip, which shows the glide instability for Fe_3Al in two angular ranges, one about the screw orientation and another at a mixed ($\theta \approx 60°$) orientation. The angular ranges for line tension instability in the nine cases are listed in Table 3.

In B2 FeAl alloys at low temperatures [19] and in $D0_3$ Fe_3Al-based alloys at elevated temperatures [29], $\{112\}\langle 111\rangle$ was reported to be an active slip system. Figure 6 shows $1/K$ plots for the three aluminides, and the angular ranges of line tension instability for this case are listed also in Table 3. With exceptions of α-Fe and Fe–40Al, edge dislocations of the $(11\bar{2})[111]$ slip system are all unstable.

2.2. Climb dislocation—prismatic loop

In Fe–35Al and in B, Cr, Pd, and W added ternary alloys, two types of thermally introduced vacancy clusters were identified by TEM [30]. They are pure prismatic faulted loops with the habit planes of {111} and {100} types. Figures 7 and 8 show the $1/K_e$ plots for these two types of prismatic loops in the three aluminides, where $K_e = K$ ($\theta = 90°$). After making a prismatic cut ($\theta = \pi/2$, the angle ϕ is defined in Fig. 1), i.e. $z \rightarrow z'$ and $x \rightarrow x'$, a rotation of the (x', y', z') coordinate system is made about the x'-axis, $\mathbf{b} = [111]/2$ or [100], away from the z'-axis, [110] or [001] direction. Table 4 lists the angular ranges of instability for Fe_3Si and six FeAl alloys.

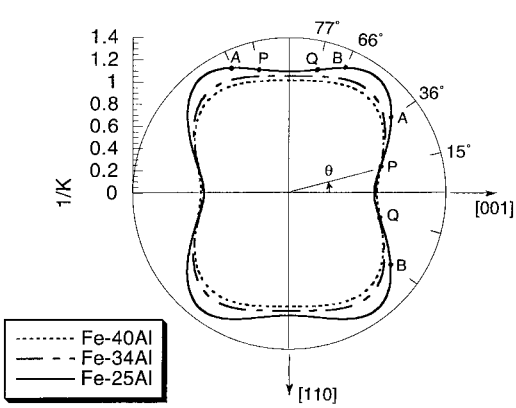

Fig. 3. Inverse energy factor plot for a $(1\bar{1}0)[001]$ glide loop in three FeAl alloys at room temperature.

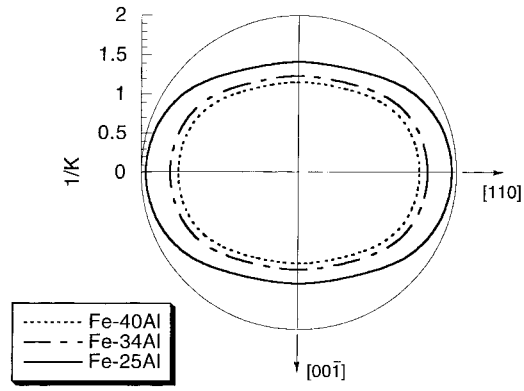

Fig. 4. Inverse energy factor plot for a $(1\bar{1}0)[110]$ glide loop in three FeAl alloys at room temperature.

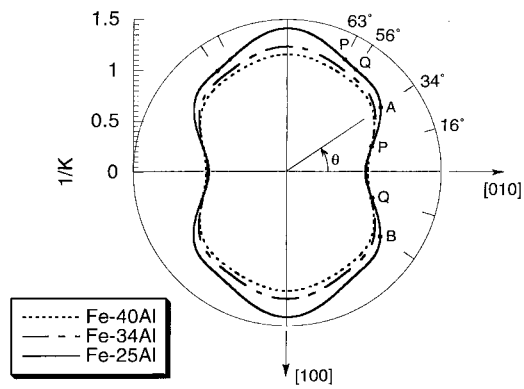

Fig. 5. Inverse energy factor plot for a (001)[010] glide loop in three FeAl alloys at room temperature.

Table 3. Angular ranges of line tension instability of (001)[010] and $(11\bar{2})[111]$ glide dislocations at room temperature. The angle θ is in deg measured counterclockwise from the slip vector

Alloy	θ_P–θ_Q (001)[010]	θ_P–θ_Q $(11\bar{2})[111]$
	$\theta = 0°$	$\theta = 90°$
α-Fe	±10	–
α-Fe[a]	±11	–
25Si	±14	±2
40Al	±15	–
34Al	±16	±2
30Al	±16	±2
30Al[a]	±16	48–54, ±6, 126–132
28Al	58–61, ±16, 119–122	48–55, ±7, 125–132
25Al	56–63, ±16, 117–124	48–56, ±7, 124–132

[a] At 773 K.

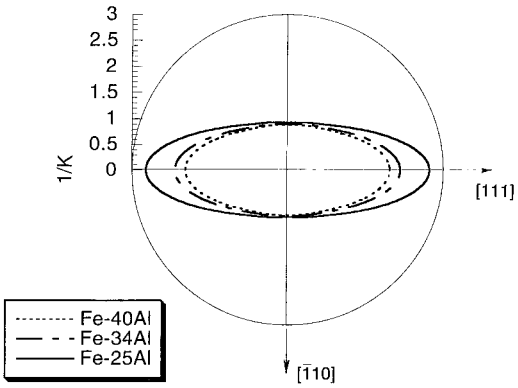

Fig. 6. Inverse energy factor plot for a (11$\bar{2}$)[111] glide loop in three FeAl alloys at room temperature.

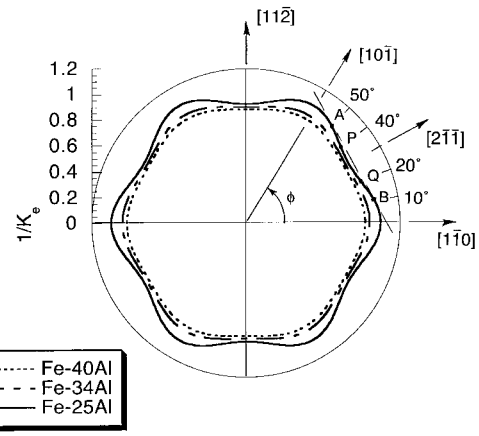

Fig. 7. Inverse energy factor plot for a (111) prismatic loop in three FeAl alloys at room temperature, $\theta = \pi/2$.

3. SCREW AND EDGE SUPERPARTIALS

The most important slip system in $D0_3$ and B2 alloys is the $\{110\}\langle 111\rangle$ type. Figure 9 shows schematically the closed loop of a (1$\bar{1}$0)[111] glide dislocation in Fe–40Al at room temperature. The so-called V-shaped dislocation bends are sketched in Fig. 9 for FeAl where the angular range of an unexposed region is $\alpha = \theta_A - \theta_B = 61° - 25° = 36°$ (Table 2). The dislocation is stable at the edge and screw orientations. The so-called stability ratio between the pure screw and edge components is $\gamma = K_e/K_s$ which is 2.1 and 2.7 for Fe–40Al and Fe_3Al, respectively, indicating that the pure screw dislocations would be energetically more favorable ($\gamma > 1.0$) [24]. The aspect ratio of the ellipse depicted in Fig. 9 is equal to this stability ratio.

3.1. Dislocation dissociations

A superdislocation of the (1$\bar{1}$0)[111] slip system in the $D0_3$ structure is dissociated into four superpartials

$$2[111] \rightarrow \mathbf{b}_1 + APB\text{-}I + \mathbf{b}_2 + APB\text{-}II + \mathbf{b}_2 + APB\text{-}I + \mathbf{b}_1 \quad (1)$$

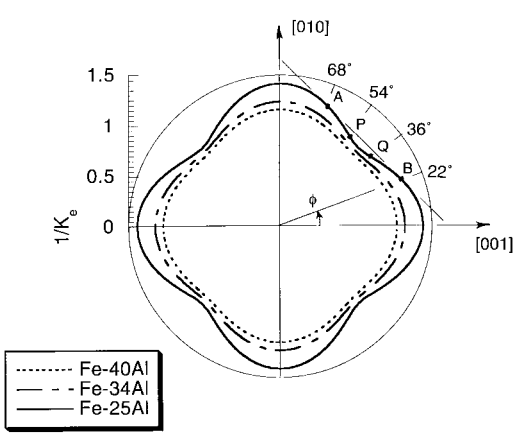

Fig. 8. Inverse energy factor plot for a (100) prismatic loop in three FeAl alloys at room temperature, $\theta = \pi/2$.

where the Burgers vectors of two types of superpartials are $\mathbf{b}_1$ or $\mathbf{b}_2 = \mathbf{b} \pm [1\bar{1}0]\xi/2 \pm [001]\eta/2$, $\mathbf{b} = [111]/2$, APB-I and APB-II are related to the nearest neighbor and the next-nearest neighbor changes, respectively, across the planar interface [31]. The B2-type and $D0_3$-type APB energies in Fe–28Al were estimated from TEM analyses to be $\Gamma_I \approx 75\ mJ/m^2$ and $\Gamma_{II} \approx 65\ mJ/m^2$ [32]. In the case of Fe_3Si at maximum $D0_3$ order, ξ and η were theoretically estimated to be about 5 and 10%, respectively [33]. Direct observation and simulation analysis of the B2-type APB interface in Fe_3Al by high resolution electron microscopy (HREM) [34] indicated that the atomic displacements at the interface in Fe_3Al are much smaller than those estimated in Fe_3Si [33]. The reason for this difference is the fact that the repulsion between Al atoms is not as strong as that between Si atoms in the $D0_3$ structure.

As the $D0_3$-to-B2 order transition occurs, Γ_{II} decreases to a value much lower than Γ_I. In a stable B2 phase, two-fold dissociation of a superdislocation occurs by

$$[111] \rightarrow \mathbf{b} + APB\text{-}I + \mathbf{b}. \quad (2)$$

It is commonly observed by TEM in deformed $D0_3$ alloys that the spacing between the inner partial

Table 4. Angular ranges of elastic instability of climb dislocations of a prismatic loop at room temperature. The angle θ is in deg measured counterclockwise from [1$\bar{1}$0] and [001]

Alloys	(111)[111] at $\phi = 30°, 90°, 150°$		(100)[100] at $\phi = 45°, 135°$	
	A–B	P–Q	A–B	P–Q
25Si	±5	–	±16	±7
40Al	±7	–	±10	±7
34Al	±11	±5	±14	±8
30Al	±11	±6	±17	±8
30Al[a]	±17	±9	±20	±9
28Al	±17	±9	±20	±9
25Al	±20	±10	±23	±9

[a] At 773 K.

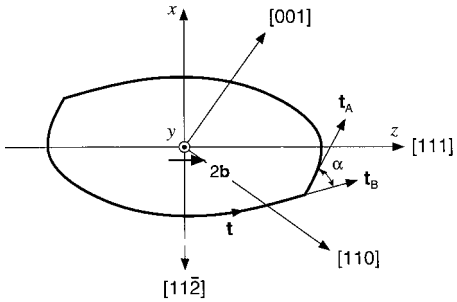

Fig. 9. Schematic drawing of the closed loop of a (1$\bar{1}$0)[111] glide dislocation in Fe–40Al at room temperature showing V-shaped bends with $\alpha = \theta_A - \theta_B = 61° - 25° = 36°$.

Table 5. Line energy factor (K) and tension factor ($K + K''$) of (1$\bar{1}$0)[111] slip dislocations in units of 10^2 GPa at room temperature

	Screw ($\theta = 0°$)		Edge ($\theta = 90°$)		
Alloys	K_s	$K_s + K_s''(\theta)$	K_e	$K_e + K_e''(\theta)$	$K_e + K_e''(\phi)$
α-Fe	0.59	2.60	1.16	0.43	1.79
α-Fe	0.53	2.33	1.04	0.39	1.60
25Si	0.56	3.09	1.22	0.48	2.42
40Al	0.51	2.76	1.08	0.47	2.12
34Al	0.46	2.85	1.04	0.46	2.39
30Al	0.41	2.53	0.91	0.41	2.13
30Al[a]	0.29	2.13	0.71	0.33	2.05
28Al	0.38	2.99	0.97	0.44	3.06
25Al	0.37	3.07	0.95	0.44	3.06

[a] At 773 K.

pair ($\mathbf{b}_2$–$\mathbf{b}_2$) bounding APB-II is much wider than those between the outer partial pairs ($\mathbf{b}_1$–$\mathbf{b}_2$) bounding APB-I [7–9, 17]. Therefore, in both $D0_3$ and B2 ordered alloys, the two-fold dissociation of equation (2) is the important starting configuration of glide dislocations in iron aluminides.

3.2. Kink-pair formation

Figure 10(a) is a schematic illustration of the small bow-out of a straight screw superpartial dislocation in the form of a kink pair with height h and length L on the (1$\bar{1}$0) glide plane. The dislocation line direction, **t**, is shown by small arrows. The elastic energy of interaction between the kinks is given by [24]

$$W_1 = \frac{b^2}{8\pi}\left[K(\theta) + \frac{\partial^2 K(\theta)}{\partial \theta^2}\right]\frac{h^2}{L} \tag{3}$$

where b is the magnitude of the Burgers vector of a superpartial and the line tension factor, $K(\theta) + K''(\theta)$, is obtained by the numerical method described in the Appendix. The energy factors, $K_s = K(\theta = 0°)$, and the line tension factors for the screw orientation are listed in Table 5 for the nine cases.

Figure 10(b) shows a situation in which a kink pair is formed on a {112} or another {110} cross-slip plane. The interaction energy in this case is given also by equation (3) with the same value of $K_s + K_s''(\theta)$ because the line tension of a ⟨111⟩ screw dislocation is independent of the glide plane and is generally positive [35]. This means that the attractive interaction between the short edge segments is the same in all cases of Fig. 10(b).

A kink pair on the edge orientation ($\theta = 90°$) is shown in Fig. 11(a). As listed in Table 5, numerical values of $K_e + K_e''(\theta)$ are much lower than those of $K_s + K_s''(\theta)$, by a factor in the range of 5.9–7.0, because the attractive interaction between the screw segments is weaker than that between the edge segments.

3.3. Jog-pair formation

A jog pair on the leading edge superpartial is illustrated in Fig. 11(b). In this case, the jog–jog interaction energy is given by making a prismatic cut at $\theta = \pi/2$ (Fig. 1) and determining the curvature of K_e with respect to ϕ

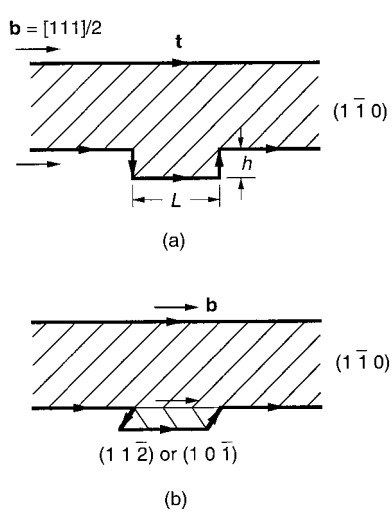

Fig. 10. Schematic drawing of two-fold dissociation of a [111] screw dislocation lying in the (1$\bar{1}$0)plane: (a) kink-pair formation in the (1$\bar{1}$0) plane; (b) kink-pair formation in one of the {112} or {101} cross-slip planes.

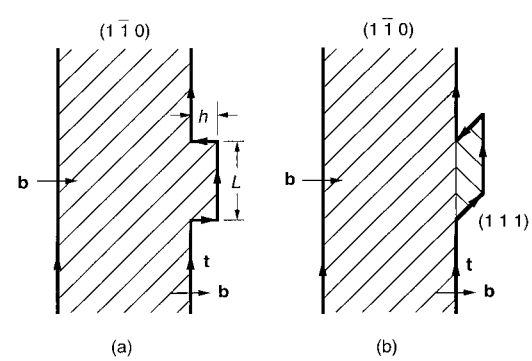

Fig. 11. Schematic drawing of two-fold dissociation of a [111] edge dislocation lying in the (1$\bar{1}$0)plane: (a) kink-pair formation in the (1$\bar{1}$0)plane; (b) jog-pair formation in the (111) plane.

$$W_2 = \frac{b^2}{8\pi}\left[K(\phi) + \frac{\partial^2 K(\phi)}{\partial \phi^2}\right]\frac{h^2}{L}. \quad (4)$$

The results of $K_e + K_e''(\phi)$ listed in Table 5 indicate that the jog–jog interaction energy is higher than the kink–kink interaction energy by a factor in the range of 4.5–7.0 for Fe–40Al to Fe–25Al with the increasing degree of elastic anisotropy.

The jog-pair formation depicted in Fig. 11(b) may occur in an uncorrelated manner with respect to such a concurrent process along the other superpartial when the equilibrium width, w_s, between the superpartials is relatively wide (i.e. Γ_I is not too high). In contrast to this case, two jog pairs of opposite sign can be formed, by short-circuit self-diffusion, along the superpartials by two different correlated processes as illustrated in Figs 12(a) and (b). The former describes the so-called climb dissociation by self-diffusion within the APB-I interface [36], and the latter is associated with possible Z-shaped bends by core diffusion along the superpartial dislocation. According to the last column of Table 5, pure edge dislocations of the $(1\bar{1}0)[111]$ slip system are stable with respect to the ϕ variation. In order to check the possibility of climb instability into Z-shaped bends along dislocations of mixed character, prismatic cuts were made at $\theta = 54.7°$ and $70.5°$ which are within the angular range of glide instability (Fig. 2) and $K + K''(\phi)$ was evaluated at $\phi = 0°$. The results show that these dislocations of mixed characters are stable against climb instability ($K + K''(\phi) > 0$).

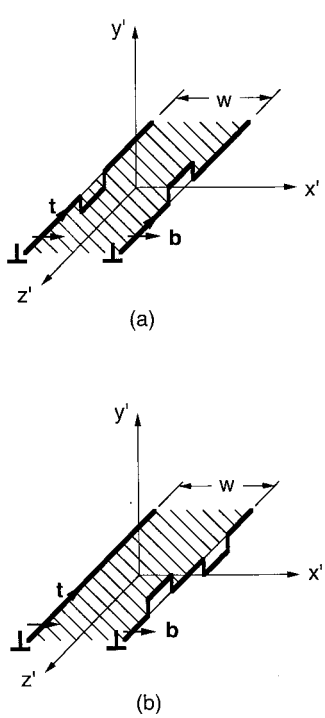

Fig. 12. Schematic drawing of correlated two jog-pair formation: (a) climb dissociation; (b) Z-shaped climb instability.

Pure edge dislocations of other slip systems were examined for climb instability also. The edge dislocations of the $(1\bar{1}0)[110]$ slip system are stable, but those of the $(11\bar{2})[111]$ and $(1\bar{1}0)[001]$ slip systems are unstable ($K + K''(\phi) < 0$). The angular ranges of climb instability for these two slip systems are the same as those given in Figs 7 and 8 and Table 4. These edge dislocations are unstable with respect to both θ and ϕ variations (Figs 3 and 8 for $(1\bar{1}0)[001]$ slip and Figs 6 and 7 for $(11\bar{2})[111]$ slip), thus corresponding to dimples of unexposed regions on the inverse energy surface [24]. Since the $\{112\} \times \langle 111\rangle$ and $\{110\}\langle 001\rangle$ slip systems operate in B2 FeAl alloys at low and high temperatures [19], respectively, the elastic instability of edge dislocations is likely to result in a V-shaped bend by glide in the former and Z-shaped bends by climb in the latter.

4. FORMATION OF PINNING POINTS

Screw and edge dislocations in B2 and $D0_3$ alloys can experience intrinsic glide resistance due to the cross-slip pinning and the APB dragging, respectively, and the driving forces for dislocation mechanisms were discussed earlier [36]. Assuming that $\{110\}$ and $\{112\}$ are the only stable APB-I planes, Saada and Veyssiére [37] prescribed the criterion for the stability of APB-dissociated $\langle 111\rangle$ screw superpartials by analyzing energy variations resulting from configurational changes. Later, using the same approach but restricting the cross slip to between the primary $\{110\}$ to twinning $\{112\}$, Sun [38] derived the specific energetic relations that exist in the transformations of dislocation configurations. These results can be incorporated into an energetic analysis for the formation of cross-slip pinning centers, Fig. 10(b), together with the kink-pair interaction energy given by equation (3). This analysis will be reported elsewhere. In the remainder of this section, we will examine the stability of pinning points on edge dislocations in terms of the energetics and kinetics of jog-pair formation.

4.1. Thermal vacancies

Effective vacancy formation enthalpies were determined to be $H_V^F = 1.04$ and 0.98 eV for Fe–37Al and Fe–39Al, respectively, and vacancy migration enthalpy was estimated to be $H_V^M = 1.7$ eV for both compositions [39]. In Fe–39Al, the equilibrium concentration of vacancies can be quite large, e.g. $c_V \approx 4.4 \times 10^{-3}$ at 1073 K, and the sum $Q^{SD} = H_V^F + H_V^M = 2.68$ eV is very close to the Fe self-diffusion enthalpy of 2.76 eV [40]. After a quench, very strong chemical (osmotic) forces are produced by vacancy supersaturation, much stronger than the climb forces usually attainable under externally applied stress [41]. For example, if all thermal vacancies in a Fe–39Al single crystal were retained after quenching from 600 to 300 K, then the supersaturation would be

$$\frac{c}{c_0} = \exp\left(\frac{H_V^F}{2kT_0}\right) \quad (5)$$

where c_0 is the equilibrium vacancy concentration at room temperature, $T_0 = 300$ K, and k is the Boltzmann constant. The corresponding chemical potential gives the climb force to be

$$F_y = \sigma_x b \cdot \frac{H_V^F}{2b^2} = \frac{K_e b}{22}. \quad (6)$$

The above estimate indicates that the chemical force generated upon quenching is equivalent to that produced by a compressive stress of $\sigma_x \cdot K_e/22 = 4.9$ GPa, which substantially exceeds the ultimate strength, 1.3 GPa, of Fe–39Al single crystals at a hard orientation [42]. This is, of course, an upper bound estimate because in practice only a small fraction of the equilibrium thermal vacancies at 600 K can be retained by using a finite quenching rate. According to the theoretical calculation in stoichiometric FeAl at 0 K [43], the divacancy binding energy is $H_{2V}^B = 0.5$ eV. This suggests that during quenching vacancies agglomerate to form divacancies and larger vacancy clusters before annihilation at dislocations, and other secondary vacancy sinks become predominant in vacancy interaction. Such vacancy clustering would lower the chemical force somewhat from the value given by equation (6). However, the chemical forces in the initial period after quenching should be of the order of 5 GPa.

4.2. Activation enthalpy for jog-pair formation

The difference in the formation enthalpy between a kink pair, Fig. 11(a), and a jog pair, of the same dimension (h, L), Fig. 11(b), consists of three terms

$$\Delta H = H_2 - H_1 = \Delta W + (\Delta\Gamma - \sigma_x b)hL \quad (7)$$

where $\Delta W = W_2 - W_1$ from equations (3) and (4), $\Delta\Gamma = \Gamma_2 - \Gamma_1$ is the difference in APB energy, and the compressive internal stress, σ_x, is directed perpendicular to the jog plane. The internal stress has two possible origins, namely, the climb stress of a mechanical origin due to the resolved normal stress component of an externally applied stress, σ, and that of a chemical origin due to the vacancy supersaturation at temperature, T

$$\sigma_x = n\sigma_x^e - \frac{kT}{\Omega}\ln\left(\frac{c}{c_0}\right) \quad (8)$$

where n is the stress concentration factor and Ω is the atomic volume. The out-of-plane component, F_y, of the elastic interaction force between the two superpartials contributes an additional term in equation (7) for the case of {112}⟨111⟩ slip [36], but not for {110}⟨111⟩ or {110}⟨001⟩ slip. In the case of (110)[111] slip, $\Delta\Gamma = \Gamma_{111} - \Gamma_{110}$.

The glide resistance in the situation described by Fig. 13 is related to the critical shear stress necessary to break away dynamically from pinning points

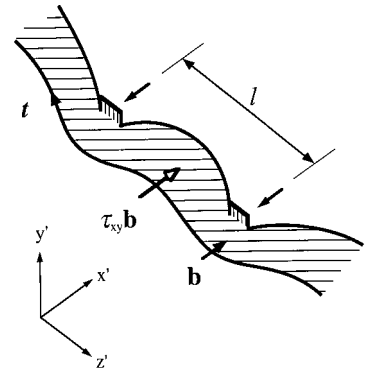

Fig. 13. Schematic drawing of pinning points formed by uncorrelated jog-pair formation under an applied stress.

$$\tau_c = \beta\frac{T_L}{bl} \quad (9)$$

where T_L is the line tension of the leading partial which depends on the internal shear stress, τ_{xy}, l is the mean spacing (linear) between pinning points, and β is a numerical factor near unity. The number density of pinning points, $N = 1/l$ can be obtained by an analysis of thermally activated formation of jog pairs

$$N = N_0 \exp\left(-\frac{\Delta H_c}{3kT}\right) \quad (10)$$

where N_0 is the number density at a reference temperature ($T_0 = 300$ K) and ΔH_c is the activation enthalpy for the formation of a jog pair. The activation enthalpy can be obtained by a numerical evaluation of the saddle point in $\Delta H = \Delta H(h, L)$ of equation (7).

5. DISCUSSION

Dislocation microstructures in both as-annealed and deformed FeAl alloys revealed by TEM are typically more complex than those in other B2 alloys such as in NiAl. The principal reason for this difference seems to be the relatively high density of grown-in dislocations in the case of FeAl alloys [44]. In Fe–40Al, grown-in dislocation microstructure varies with the quenching and aging temperatures in the types of perfect loops, square helices, paired helices connected to an APB, and others [45]. Nevertheless, square dislocation loops of the {001}⟨001⟩ type (Fig. 8) were directly observed in Fe–47.5Al after high-temperature extrusion [46], in Fe–39Al after quenching from 1173 K and annealing at 698 K [47], and in Fe–40Al–0.6C alloys quenched and aged at 673 K [48]. Z-shaped dislocation bends were also observed along the helical segment of ⟨001⟩ dislocations in the extruded alloys [46]. Quenched-in prismatic loops of the {111}⟨111⟩ type (Fig. 7) observed in Fe–35Al–1W [30] were too large (1–2 μm in diameter in thin foils of ~200 nm

thickness) to reveal the predicted six-fold faceting. Under an applied stress, these and other types of dislocation bundles often evolve and emerge as heterogeneous sources for the multiplication of ⟨111⟩ and ⟨001⟩ type glide dislocations [44].

The available TEM data of deformed microstructures are consistent with the stability of the glide dislocations in FeAl calculated in this paper. After compressive deformation of Fe–47.2Al single crystals at high temperatures (470–1000 K), Umakoshi and Yamaguchi [49] investigated TEM foils parallel to the observed slip planes. Primary dislocations of the $(1\bar{1}0)[001]$ slip system were observed to be mostly edge or mixed character, and many of them were seen to have sharp V-shaped bends (Fig. 10 of Ref. [49]). This result is entirely consistent with the glide instability predicted by Fig. 3 and Table 2. A TEM analysis was made in Fe–39.5Al single crystals after compression at 883 K [6], and the prevalence of edge and near-edge (001)[010] dislocations is shown in Fig. 13 of Ref. [6]. Dislocation arrangements in a Fe–47.2Al crystal deformed by (001)[010] slip at 773 K consists of edge dipoles and numerous small loops elongated perpendicular to the [010] direction (Fig. 8 of Ref. [49]). The absence of screw and near-screw dislocations in these microstructures is consistent with Fig. 5 and Table 3.

Many TEM micrographs of [111] dislocation substructures in the $(\bar{1}01)$ foils prepared from FeAl single crystals deformed by the primary $(\bar{1}01)[111]$ slip system have been reported [6, 16, 20, 42, 49, 50] at room temperature and elevated temperatures (e.g. 773 K). Dislocations in the deformed microstructures of B2 FeAl alloys are observed to be aligned, in general, outside of the instability range of $25^\circ < \theta < 61^\circ$ for Fe–40Al and $25^\circ < \theta < 75^\circ$ for Fe_3Al (Table 2), showing essentially as many edge and near-edge orientations as screw and near-screw orientations. In the case of B2 FeAl alloys, some sharp corners were often noticed, e.g. in Fe–39Al deformed at 823 K [50]. However, V-shaped bends of $36^\circ < \alpha < 50^\circ$ (Table 2) are not clearly identified in FeAl alloys as they were in the case of β-CuZn [27]. In the case of Fe–44Al strengthened by excess vacancies [51], a cellular microstructure consisting of dipoles and multipoles was developed with the preferred alignment along the [101] direction which is roughly perpendicular to the direction of the instability range.

A full analysis of the magnitude and spatial dependence of the internal stress tensor with respect to a reference coordinate system (say, the primary slip system shown in Fig. 9) is the important step for characterizing the relationship between as-annealed dislocation microstructures and deformation mechanisms. While the glide stress, τ_{yz}, is the thermodynamic driving force ($F = 2\tau_{yz}b$ in Fig. 9) for expansion of the closed loop, several non-glide stress components will assist thermally activated dislocation mechanisms to work and thus impede the kinetics of loop expansion [36]. The cross-slip pinning at the screw orientation ($\mathbf{t} = \pm[111]$) is effected by the τ'_{yz} component on the cross-slip plane (Fig. 10). The compressive stress (σ'_x in Fig. 11 and σ_z in Fig. 9) plays an important role in pinning of the edge dislocation ($\mathbf{t} = \pm[11\bar{2}]$). In addition, the tendency for a glide decomposition in the orientation range between $\mathbf{t} = [110]$ and [001] is controlled by the sign and magnitude of τ_{xy}. The initial grown-in dislocation microstructure with respect to the primary slip system is the key information necessary for an internal stress analysis, particularly for FeAl alloys in which the formation and clustering of thermal vacancies [43] are prevalent, but this information is seldom available.

The activation energy analysis for a jog-pair formation will depend on the input variables into the three terms in equation (7). The first term is obtained by putting the numerical values from the last two columns of Table 5 into equations (3) and (4) for Fe_3Si and seven different FeAl alloys. The second term requires knowledge of anisotropic APB energies that may depend on the alloy composition and temperature. The vacancy supersaturation is the most difficult to estimate especially because of the apparent heterogeneity of internal stress in the microstructure. This analysis pertaining to the edge component of a glide loop needs to be combined with the similar analysis for a kink-pair formation at the screw component in order to determine the overall glide resistance against dislocation loop multiplication at the Frank–Read source. This project is under way, and the results will be reported elsewhere.

6. SUMMARY

1. Elastic instability of glide and prismatic loops in α-Fe, Fe_3Si, and seven FeAl alloys at room temperature and 773 K was examined by numerically calculating the anisotropic energy factor and line tension for a straight dislocation.
2. A wide variety of dislocation microstructures revealed in TEM micrographs of as-annealed and deformed FeAl single crystals available in the literature are all consistent with the calculated results of the present analysis.
3. Activation enthalpy for the formation of a jog pair was derived by incorporating the differences in elastic interaction energies, APB energies, and internal climb stresses, and the critical shear stress for dynamic break-away from pinning points was prescribed.
4. Glide resistance to a closed dislocation loop of the primary {110}⟨111⟩ slip was discussed by including the cross-slip pinning of the screw component and the possible glide decomposition

over near-edge orientations, and the important role of internal stress tensor was emphasized.

Acknowledgements—The authors thank E. P. George and J. A. Horton for helpful comments on the manuscript. This research was sponsored by the Division of Materials Sciences, Office of Basic Energy Sciences, U.S. Department of Energy under contract number DE-AC05-96OR22464 with Lockheed Martin Energy Research Corp., and also supported in part by the program of Japan Society for the Promotion of Science Postdoctoral Fellowships for Research Abroad.

REFERENCES

1. Schneibel, J. H. and Crimp, M. A. (ed.), *Processing, Properties, and Applications of Iron Aluminides*. TMS, Warrendale, PA, 1994.
2. Deevi, S. C., Morris, D. G., Schneibel, J. H. and Sikka, V. K., *Mater. Sci. Engng*, 1998, **A258**, 1.
3. Rieu, J. and Goux, C., *Mém. scient. Revue Métall.*, 1969, **65**, 689.
4. Nagpal, P. and Baker, I., *Metall. Trans. A*, 1990, **21**, 2281.
5. Carleton, R., George, E. P. and Zee, R. H., *Intermetallics*, 1995, **3**, 433.
6. Yoshimi, K., Hanada, S. and Yoo, M. H., *Intermetallics*, 1996, **4**, S159.
7. Schröer, W., Hartig, C. and Mecking, H., *Z. Metallk.*, 1993, **84**, 294.
8. Rösner, H., Molénat, G., Kolbe, M. and Nembach, E., *Mater. Sci. Engng A*, 1995, **192/193**, 793.
9. Král, F., Schwander, P. and Kostorz, G., *Acta mater.*, 1997, **45**, 675.
10. Morris, D. G., *Phil. Mag. A*, 1995, **71**, 1281.
11. Yoshimi, K., Hanada, S. and Yoo, M. H., in *High-Temperature Ordered Intermetallic Alloys VII*, ed. C. C. Koch, C. T. Liu, N. S. Stoloff and A. Wanner, *MRS Symp. Proc.*, Vol. 460. MRS, Pittsburgh, PA, 1996, p. 313.
12. George, E. P. and Baker, I., *Phil. Mag. A*, 1998, **77**, 737.
13. Crawford, R. C., Ray, T. L. F. and Cockayne, D. J. H., *Phil. Mag.*, 1973, **27**, 1.
14. Leamy, H. J., Gibson, E. D. and Kayser, F. X., *Acta metall.*, 1967, **15**, 1827.
15. Yoo, M. H., Köppe, M., Hartig, C., Mecking, H., Hermann, W. and Sockel, H.-G., *Acta mater.*, 1997, **45**, 4323.
16. Crimp, M. A. and Vedula, K., *Phil. Mag. A*, 1991, **63**, 559.
17. Perez, J. F. and Morris, D. G., *Phil. Mag. A*, 1996, **74**, 665.
18. Fu, C. L. and Yoo, M. H., *Acta metall. mater.*, 1992, **40**, 703.
19. Yoo, M. H., Takasugi, T., Hanada, S. and Izumi, O., *Mater. Trans. JIM*, 1990, **31**, 435.
20. Yoshimi, K., Matsumoto, N., Hanada, S. and Yoo, M. H., in *Processing, Properties, and Applications of Iron Aluminides*, ed. J. H. Schneibel and M. A. Crimp. TMS, Warrendale, PA, 1994, p. 205.
21. Umakoshi, Y. and Yamaguchi, M., *Phil. Mag. A*, 1981, **44**, 711.
22. Mendiratta, M. G., Kim, H. M. and Lipsitt, H. A., *Metall. Trans.*, 1984, **15A**, 395.
23. Kad, B. K. and Horton, J. A., *Mater. Sci. Engng A*, 1997, **239/240**, 118.
24. Wang, L. and Lothe, J., *Phil. Mag. A*, 1995, **71**, 395.
25. Leese, J. and Lord, A. E., *J. appl. Phys.*, 1968, **39**, 3986.
26. Rausch, J. B. and Kayser, F. X., *J. appl. Phys.*, 1977, **48**, 487.
27. Head, A. K., *Physica status solidi*, 1967, **19**, 185.
28. Friedel, J., *Dislocations*. Pergamon Press, Oxford, 1964, p. 32.
29. Kad, B. K., Schoenfeld, S. E., Asaro, R. J., McKamey, C. G. and Sikka, V. K., *Acta mater.*, 1997, **45**, 1333.
30. Yoshimi, K., Hanada, S., Onuma, T. and Yoo, M. H., *Phil. Mag. A*, 1996, **73**, 443.
31. Yamaguchi, M. and Umakoshi, Y., *Prog. Mater. Sci.*, 1990, **34**, 21.
32. Crawford, R. C. and Ray, I. L. F., *Phil. Mag.*, 1977, **35**, 549.
33. Paidar, V., *Czech. J. Phys. B*, 1976, **23**, 865.
34. Shindo, D., Yoo, M. H., Hanada, S. and Hiraga, K., *Phil. Mag. A*, 1991, **64**, 1281.
35. Sun, Y. Q. and Ngan, A. H. W., *Phil. Mag. Lett.*, 1996, **74**, 175.
36. Yoo, M. H., Horton, J. A. and Liu, C. T., *Acta metall.*, 1988, **36**, 2935.
37. Saada, G. and Veyssiére, P., *Physica status solidi (b)*, 1992, **172**, 309.
38. Sun, Y. Q., *Acta metall. mater.*, 1995, **43**, 3775.
39. Würschum, R., Grupp, C. and Schaefer, H.-E., *Phys. Rev. Lett.*, 1995, **75**, 97.
40. Mehrer, H., *Mater. Trans. JIM*, 1996, **37**, 1259.
41. Hirth, J. P. and Lothe, J., *Theory of Dislocations*, 2nd edn. Wiley-Interscience, New York, 1982, pp. 91 and 612.
42. Yoshimi, K., Hanada, S. and Yoo, M. H., *Intermetallics*, 1996, **4**, 159.
43. Fu, C. L., Ye, Y.-Y., Yoo, M. H. and Ho, K. M., *Phys. Rev. B*, 1993, **48**, 6712.
44. Yoo, M. H., Appel, F., Wagner, R. and Mecking, H., in *Deformation and Fracture of Ordered Intermetallic Materials III*, ed. W. O. Soboyejo, T. S. Srivatsan and H. L. Fraser. TMS, Warrendale, PA, 1996, p. 3.
45. Junqua, N., Desoyer, J. C. and Moine, P., *Physica status solidi (a)*, 1973, **18**, 387.
46. Feng, C. R. and Sadananda, K., *Scripta metall. mater.*, 1990, **24**, 2107.
47. Yoshimi, K., Unpublished work, 1998.
48. Pang, L. and Kumar, K. S., *Acta mater.*, 1998, **46**, 4017.
49. Umakoshi, Y. and Yamaguchi, M., *Phil. Mag.*, 1980, **41**, 573.
50. Yoshimi, K., Yoo, M. H. and Hanada, S., *Acta mater.*, 1998, **46**, 5769.
51. Yoshimi, K., Saeki, Y., Yoo, M. H. and Hanada, S., *Mater. Sci. Engng*, 1998, **A258**, 75.
52. Stroh, A. N., *Phil. Mag.*, 1958, **3**, 625.
53. deWit, G. and Koehler, J. S., *Phys. Rev.*, 1959, **116**, 1113.

APPENDIX

The elastic energy per unit length of a straight dislocation in an elastically anisotropic crystal is given by [41]

$$E = \frac{Kb^2}{4\pi}\ln\left(\frac{R}{r_0}\right) \tag{A1}$$

where b is the magnitude of the Burgers vector, R and r_0 are the outer and inner cut-off radii in the continuum description of dislocations, and K is the energy factor which is a function of the elastic constants of the crystal and the orientation of dislocation coordinate axes with respect to the crystal axes. For an isotropic medium, K is given as a function of the angle θ between the Burgers vector and the dislocation line (Fig. 1) as follows:

$$K = \mu\left(\cos^2\theta + \frac{\sin^2\theta}{1-\nu}\right) \tag{A2}$$

where μ is the shear modulus and ν is Poisson's ratio. For an arbitrary orientation of the dislocation in an anisotropic crystal, K is obtained numerically on the basis of the sextic formalism by Stroh [52].

The calculated results of $K(\theta)$ for θ in the interval $(0, \pi)$ are represented by a Fourier series

$$K_n \approx \sum_{n=0}^{N}[a_n \cos(2n\theta) + b_n \sin(2n\theta)] \tag{A3}$$

where a_n and b_n are functions only of the elastic constants, not of θ. These coefficients are determined by

$$a_n = \frac{2}{\pi}\int_0^{\pi} K(\theta)\cos(2n\theta)\,\mathrm{d}\theta \tag{A4}$$

$$b_n = \frac{2}{\pi}\int_0^{\pi} K(\theta)\sin(2n\theta)\,\mathrm{d}\theta. \tag{A5}$$

The series up to $N = 12$ is found to be sufficient to give the difference between K_n and K to be $(K_n - K)/K < 10^{-6}$. The second derivative of K_n with respect to θ is given by

$$K_n'' = -4\sum_{n=0}^{N} n^2[a_n \cos(2n\theta) + b_n \sin(2n\theta)] \tag{A6}$$

and the line tension is obtained by inserting equations (A3) and (A6) into the following expression [53]:

$$T_{\mathrm{L}} = \frac{b^2}{4\pi}\ln\left(\frac{R}{r_0}\right)(K_n + K_n''). \tag{A7}$$